IEEE *Access*

Multidisciplinary : Rapid Review : Open Access Journal

Study of the Extended Phase Shift Migration for Three-Dimensional MIMO-SAR Imaging in Terahertz Band

HANG GAO[1,2,3], CHAO LI [1,2,3], SHIYOU WU [1,2], HEBIN GENG[1,2,3], SHEN ZHENG[1,2], XIAODONG QU [1,2], AND GUANGYOU FANG[1,2,3]

[1]Aerospace Information Research Institute, Chinese Academy of Sciences, Beijing 100190, China
[2]Key Laboratory of Electromagnetic Radiation and Sensing Technology, Chinese Academy of Sciences, Beijing 100190, China
[3]School of Electronic, Electrical and Communication Engineering, University of Chinese Academy of Sciences, Beijing 100190, China

Corresponding author: Chao Li (cli@mail.ie.ac.cn)

ABSTRACT In this paper, the extended phase shift migration (PSM) for three-dimensional (3-D) multi-input-multi-output synthetic aperture radar (MIMO-SAR) imaging in terahertz (THz) band was studied. Based on one-dimensional MIMO arrays combined with synthetic aperture scan along another dimension, MIMO-SAR imaging scheme allows the number of array elements to be greatly reduced compared with the two-dimensional (2-D) MIMO arrays. By analyzing the derived analytical expression of the scattered waves in the frequency-wavenumber domain, the MIMO-SAR data in a certain frequency is mapped to another frequency of the 'explode fields' of the monostatic form in accordance with a newly defined 3-D dispersion relations. By multiplying the modified phase shift terms in each frequency of 'explode fields', the 'explode fields' at different range planes can be reconstructed. Finally, the 'explode fields' at time t = 0 can be successfully derived to realize fast imaging reconstruction for MIMO-SAR, with great reduction on the time consuming as compared with the BP algorithm and better accuracy compared with the Stolt migration. Additionally, due to its iterative nature in the range direction, the proposed algorithm is more flexible in treating more complicated scenarios, such as the image reconstruction in the multi-layer medium. A bistatic prototype imager was designed for the proof-of-principle experiments in THz band. The 3-D imaging results of different targets and computational complexity were also given to demonstrate the good performance of the proposed algorithm for THz MIMO-SAR imaging.

INDEX TERMS Terahertz (THz), three-dimensional imaging, multi-input-multi-output synthetic aperture radar (MIMO-SAR), phase shift.

I. INTRODUCTION

Terahertz (THz) waves are generally referred to the spectrum from 0.1 to 10 THz, which lie in the gap between the microwave and infrared. THz has many advantages due to its unique electromagnetic wave band. Unlike optical and infrared radiation, THz waves offer the property of being able to 'see through' obscuring materials such as clothing, cardboard, plastics, and wood with relatively little loss. Compared with microwaves and lower radio frequency waves, THz

waves have shorter wavelengths and broader bandwidths, which result in better spatial resolutions and make the objects easier to be identified. Especially and attractively, resolutions in millimeter even sub-millimeter level for all the three spatial dimensions are available for an active imaging system in THz band, which is found to be promising for plenty of applications [1]–[10], such as security and safety screening, non-destructive testing (NDT) and evaluation.

Limited by the techniques and the costs of THz sources and detectors, imaging systems in the early stage were usually developed based on single transceiver with optical-mechanical scanners. For example, the Jet Propulsion

The associate editor coordinating the review of this manuscript and approving it for publication was Thomas Kuerner .

Laboratory (JPL) group developed a 3-D imaging radar in FMCW scheme at the band of 0.675 THz, by employing a large focusing elliptical reflector combined with a small rotating sub reflector to cover the two-dimensional (2-D) field of view (FOV) [5]–[7]. Imaging system with similar architecture was also studied in 0.35 THz by the Pacific Northwest National Laboratory (PNNL) [8]. Additionally, scanning quasi-optics with comparatively compact size by embedding both focusing and scanning reflectors inside a pair of parallel metal plates was also proposed to achieve 3-D imaging in THz band with a single transceiver [11], [12].

As the ever growing of the security and NDT requirements, active THz imaging with higher data acquisition speed becomes more and more necessary, especially for real-time applications in high throughput scenarios. In recent years, many efforts have been made on THz active imaging with multi-pixel parallel detection based on transceiver arrays [13]–[18]. For example, the JPL group has integrated a small array into its FMCW radar system to improve imaging speed [14], [15]. More intuitively, another way with the concept of multi-input-multi-output (MIMO) array was lately introduced to achieve much higher array efficiency for active imaging in THz band [16]–[18]. A MIMO array based side-looking imaging system without scanning mechanism was studied in [16], which has a fast imaging speed but lacks 3-D imaging capabilities. Another 0.36 THz system employs a one-dimensional (1-D) MIMO array combined with a scanning quasi-optics to cover another dimension of the FOV. With the MIMO architecture, the total elements of the transceivers can be significantly reduced as compared with the conventional array topology. And the concept of the synthetic aperture can be implemented in the MIMO array dimension with adaptive focusing. However, the fixed imaging distance is still expected in this imaging topology in [17], [18], since real aperture focusing is used in the quasi-optical scanning dimension.

For the purpose to achieve a fully adaptive focusing in THz band with high array efficiency, a multi-input-multi-output synthetic aperture radar (MIMO-SAR) imaging scheme with novel imaging reconstruction method is studied in this paper. As the schematic shown in Fig.1, the 2-D FOV in x-y plane was covered by the scan of the 1-D MIMO array (x-direction) along the other dimension (y-direction). Reconstruction of images can be implemented by the combination of MIMO array signal processing and synthetic aperture thesis in the corresponding dimensions. For 3-D image reconstruction with the complex bistatic MIMO-SAR data, the methods based on coherent summations or convolutions with phase-corrected or time-compensated signals can be implemented, such as the conventional back projection (BP) algorithm [19] and the Modified Kirchhoff algorithm [20], [21]. However, such kind of methods are usually time consuming with heavily limited applications, especially for real-time imaging.

So far, few works have been reported on fast reconstruction methods for the 3-D MIMO-SAR imaging. To accelerate imaging reconstruction, the kernel of BP algorithm

is approximately separated into two independent kernels for the effective application of fast Fourier transformation (FFT) [22]. However, the approximation results in obvious degradations in the reconstructed point spread function (PSF) although the consumed time is reduced. Additionally, a 3-D MIMO near-field range migration algorithm (RMA) with high efficiency was proposed by Zhuge based on 2-D MIMO array in [23], which reduced the computational complexity greatly as compared with the conventional BP algorithm. It was then extended to the MIMO-SAR regime by utilizing the spherical wave decomposition by Zhu in [24]. These wavenumber domain algorithms based on Stolt interpolation are usually efficient in dealing with the image reconstruction in single medium with the constant wave speed condition [25]. More recently, two Modified Kirchhoff based frequency domain algorithms were also proposed in [26]. Similar to Zhu's method, the first algorithm is also based on the Stolt interpolation. The second algorithm decomposes the MIMO imaging problem into several single-input-multiple-output (SIMO) problems, which allows a more flexible distribution of the transmitters, but at the cost of time-consuming problems.

In this paper, the phase shift migration was studied for the MIMO-SAR reconstruction with high efficiency, and high accuracy, which is also suitable for more complex imaging scenes such as image reconstruction for targets embedded in multi-layer medium. The phase shift migration is originated from the exploding reflector model in reflection seismology [27]–[29] and usually implemented in monostatic imaging [25], [30], [31]. Compared with the BP algorithm, the proposed MIMO-SAR PSM algorithm has a great reduction on time consuming in reconstructing the images by using FFT operations. Taking advantages of its non-interpolation feature, PSM has higher numerical accuracy compared with Stolt migration for reconstructing high resolution images. Additionally, due to its iterative nature in range direction, PSM is more flexible in treating more complicated scenarios, such as image reconstruction in the multi-layer medium. The proposed methods and the algorithms were verified by the proof-of-principle experiments in THz band.

This paper is organized as follows. The theory and the algorithm of the MIMO-SAR PSM algorithm are presented in Section II. Several implementation issues including sampling criteria, spatial resolution, implementation details and computational complexity are discussed in Section III. In Section IV and V, numerical simulation and experimental results are given in THz band respectively, through which the effectiveness and the efficiency of the proposed algorithm are demonstrated. Finally, a conclusion is drawn in Section VI.

II. FORMULATION
A. THEORY AND ALGORITHM OF THE EXTENDED PSM FOR MIMO-SAR

As given in Fig.1, the locations of the transmitters and receivers are denoted as (x_t, y, z) and (x_r, y, z), respectively.
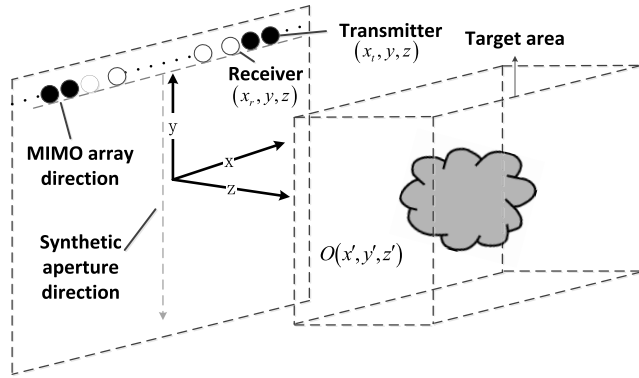
FIGURE 1. Imaging system geometry of the MIMO-SAR configuration.

The radiation aperture of linear MIMO array is assumed locating at a plane z and scanned along y axis forming a planar aperture to get the echoed field $s(x_t, x_r, y, z, \omega)$. Assume that the imaging domain is homogeneous and represented as D in the following content. The general target has a reflectivity distribution function $O(x', y', z')$. Under such MIMO-SAR imaging regime, the corresponding scattered wave field can be expressed as

$$
\begin{aligned}
& s(x_t, x_r, y, z, \omega) \\
& = \iiint_D O(x', y', z') \frac{\exp(-jkR_t)}{4\pi R_t} \cdot \frac{\exp(-jkR_r)}{4\pi R_r} \cdot dx' dy' dz'
\end{aligned}
$$

(1)

where ω is the angular frequency, $k = \omega/c_0$ is the usual wavenumber in free space, and c_0 is the propagation speed of electromagnetic waves in free space. R_t and R_r are the distances from each point of the target to transmitters and receivers respectively, which are expressed as.

$$
R_t = \sqrt{(x_t - x')^2 + (y - y') + (z - z')^2}
$$

(2)

$$
R_r = \sqrt{(x_r - x')^2 + (y - y') + (z - z')^2}
$$

(3)

By ignoring the amplitude decay factors which has little impact on THz image reconstruction, the scattered data can be simplified as

$$
\begin{aligned}
& s(x_t, x_r, y, z, \omega) \\
& = \iiint_D O(x', y', z') \exp(-jk(R_t + R_r)) dx' dy' dz'
\end{aligned}
$$

(4)

Fourier transformations was then carried out on both sides of (4) along x_t, x_r and y dimensions which correspond to the spatial frequency k_{xt}, k_{xr}, k_y respectively. Then we got

$$
\begin{aligned}
& \tilde{s}(k_{xt}, k_{xr}, k_y, z, \omega) \\
& = \iiint_D O(x', y', z') \cdot F(k_{xt}, k_{xr}, k_y, \omega) dx' dy' dz'
\end{aligned}
$$

(5)

where

$$
\begin{aligned}
F(k_{xt}, k_{xr}, k_y, \omega) = & \iiint \exp(-jk(R_t + R_r)) \cdot \exp(-jk_y y) \\
& \cdot \exp(-jk_{xt} x_t) \cdot \exp(-jk_{xr} x_r) dy dx_t dx_r
\end{aligned}
$$

(6)

The Method of Stationary Phase (MSP) was utilized in dealing with the 3-D integration in (6), and the solution is shown as

$$
\begin{aligned}
& F(k_{xt}, k_{xr}, k_y, \omega) \\
& = \exp(-j(k_{xt} + k_{xr}) x' - jk_y y') \\
& \cdot \exp\left(-j\left(\sqrt{\left(\sqrt{k^2 - k_{xt}^2} + \sqrt{k^2 - k_{xr}^2}\right)^2 - k_y^2}\right)(z' - z)\right)
\end{aligned}
$$

(7)

By substituting (7), (5) can be expressed as

$$
\begin{aligned}
& \tilde{s}(k_{xt}, k_{xr}, k_y, z, \omega) \\
& = \iiint_D O(x', y', z') \exp(-j(k_{xt} + k_{xr}) x' - jk_y y') \\
& \cdot \exp\left(-j\left(\sqrt{\left(\sqrt{k^2 - k_{xt}^2} + \sqrt{k^2 - k_{xr}^2}\right)^2 - k_y^2}\right.\right. \\
& \left.\left. \times (z' - z)\right)\right) dx' dy' dz'
\end{aligned}
$$

(8)

A further simplified expression can be obtained if we define the new 3-D dispersion relations as

$$
\begin{cases}
\hat{k}_x = k_{xt} + k_{xr} \\
\hat{k}_z = \sqrt{\left(\sqrt{k^2 - k_{xt}^2} + \sqrt{k^2 - k_{xr}^2}\right)^2 - k_y^2} \\
\hat{\omega} = \dfrac{c_0 \sqrt{\hat{k}_x^2 + k_y^2 + \hat{k}_z^2}}{2}
\end{cases}
$$

(9)

Then (8) was simplified as

$$
\begin{aligned}
& \tilde{s}(k_{xt}, k_{xr}, k_y, z, \omega) \\
& = \iiint_D \exp\left[-j\left(\hat{k}_x x' + k_y y' + \hat{k}_z (z' - z)\right)\right] \\
& \cdot O(x', y', z') dx' dy' dz'
\end{aligned}
$$

(10)

Comparing (8) with Eq. (7) in [30], we can find that the frequency domain "explode field" of the MIMO-SAR regime is ready to derive if we reorganize the left side of (10) according to (9) into

$$
\begin{aligned}
& \tilde{U}(\hat{k}_x, k_y, z, \hat{\omega}) \\
& = \iiint_D \exp\left[-j\left(\hat{k}_x x' + k_y y' + \hat{k}_z (z' - z)\right)\right] \\
& \cdot O(x', y', z') dx' dy' dz'
\end{aligned}
$$

(11)

It's interesting to find that, after employing several Fourier transformations and data rearrangement in spatial frequency

domain, the bistatic MIMO-SAR data $\tilde{s}$ measured in a certain frequency ω is equivalent to the frequency domain 'explode fields' $\tilde{U}$ in an 'equivalent frequency' $\hat{\omega}$ as shown in (11). The detailed expression of the 'equivalent frequency' $\hat{\omega}$ is given as:

$$\frac{\hat{\omega}}{\omega} = \frac{1}{\sqrt{2}}\sqrt{\left(1 + k'_{xt}k'_{xr}\right) + \left(1 - k'_{xt}k'_{xr}\right)\sqrt{1 - \left(\frac{k'_{xt} - k'_{xr}}{1 - k'_{xt}k'_{xr}}\right)^2}} \tag{12}$$

where $k'_{xt} = k_{xt}/k$, and $k'_{xr} = k_{xr}/k$ are referred as the normalized wavenumbers of transmitting and receiving arrays, respectively. And $\hat{\omega}/\omega$ is referred as the normalized equivalent frequency. Fig.2 illustrates the variation of the normalized equivalent frequency as a function of the two normalized wavenumbers. It's interesting to find that, as the wavenumbers for transmitting and receiving arrays come close to each other, the 'equivalent frequency' $\hat{\omega}$ approaches the working frequency ω, and as the difference between the two wavenumbers increases, the value of the 'equivalent frequency' $\hat{\omega}$ becomes smaller.
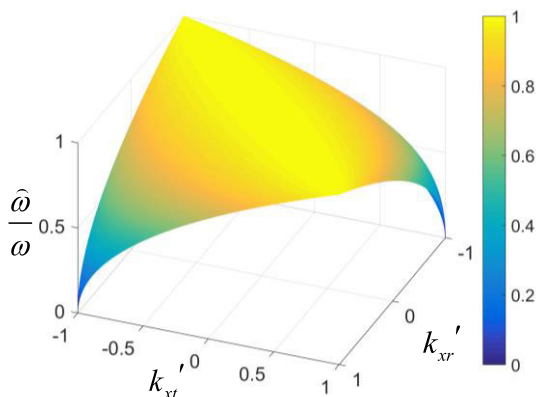

FIGURE 2. The variation of the normalized equivalent frequency as a function of the two normalized wavenumbers of the transmitting and the receiving arrays.

We can also find the extrapolation property in range direction of the frequency domain 'explode fields' of the MIMO-SAR regime from (11), which means, the frequency domain 'explode fields' of different range planes in the modified frequency-wavenumber domain can be obtained according to bistatic MIMO-SAR data measured in z plane as

$$\tilde{U}\left(\hat{k}_x, k_y, z_i, \hat{\omega}\right) = \tilde{U}\left(\hat{k}_x, k_y, z, \hat{\omega}\right)\exp\left[j\hat{k}_z(z_i - z)\right] \tag{13}$$

where $z_i = z_0, z_1, \ldots z_{n1}$ represents different range planes in the FOV. $\exp[j\hat{k}_z(z_i - z)]$ is defined as the phase shift term in the MIMO-SAR regime.

The 'explode field' in each z_i plane can finally be derived based on the 2-D inverse Fourier transform in the modified wavenumber domain

$$U(x, y, z_i, \hat{\omega}) = \iint \tilde{U}(\hat{k}_x, k_y, z_i, \hat{\omega})\exp[j(\hat{k}_x x + k_y y)]d\hat{k}_x dk_y \tag{14}$$

According to the thesis of the exploded reflector model, the "explode field" at time $t = 0$ has a similar form as the object to be imaged [30]. Therefore, the reconstructed image can be finally recovered by the following integration over the 'equivalent frequency' $\hat{\omega}$

$$u(x, y, z_i, t)\mid_{t=0} = \int U(x, y, z_i, \hat{\omega})d\hat{\omega} \tag{15}$$

In summary, a comprehensive PSM algorithm can be extended for the MIMO-SAR regime based on the data rearrangement and extrapolation with the modified phase shift terms in modified wavenumber domain and integration over the 'equivalent frequency'. The concluded expression is shown as

$$u(x, y, z_i, t)\mid_{t=0} = \int FT_{2D}^{-1}\left\{FT_{3D}\left[s\left(x_t, x_r, y, z, \omega\right)\right]\right.$$
$$\left. \times \exp\left[j\hat{k}_z(z_i - z)\right]\right\}_{reorganize} d\hat{\omega} \tag{16}$$

Compared with the BP algorithm, the proposed MIMO-SAR PSM algorithm has a great reduction on the time consuming by effectively employing the FFT operations. Compared with the Stolt migration algorithm, the proposed MIMO-SAR PSM has better accuracy by avoiding the numerical interpolation in the wavenumber domain. The performance of this algorithm will be illustrated in detail in the following Sections.

III. IMPLEMENTATION ISSUES
A. SAMPLING CRITERIA AND SPATIAL RESOLUTION
The sampling criteria of the MIMO-SAR regime should both satisfy the Nyquist sampling criteria in the MIMO array direction [23] as well as the Nyquist sampling criteria in the synthetic aperture scan direction [33] to avoid aliasing

$$\begin{cases} d_{xt} \leq \lambda_{\min}\dfrac{\sqrt{(L_{xt} + D_x)^2/4 + z_0^2}}{L_{xt} + D_x} \\ d_{xr} \leq \lambda_{\min}\dfrac{\sqrt{(L_{xr} + D_x)^2/4 + z_0^2}}{L_{xr} + D_x} \\ d_y \leq \dfrac{\lambda_{\min}}{\min(4\sin(\theta_{HBW}/2), 2D_y/z_0)} \end{cases} \tag{17}$$

where d_{xt}, d_{xr} and d_y are the intervals of the transmitters, receivers and the synthetic aperture scan path, and L_{xt}, L_{xr} and L_y are the length of transmitting array, receiving array and the synthetic aperture length respectively. $\lambda_{\min}$ is the smallest wavelength which corresponds to the maximum frequency within the data bandwidth, D_x and D_y are width for the FOV in x and y directions, z_0 is the minimum distance between the array plane and the FOV and θ_{HBW} is the half beam width (HBW) of antennas.

The spatial resolution of this algorithm is approximately shown in (18) which is a combined result of previous work [22], [26], [32] due to the combination feature of this
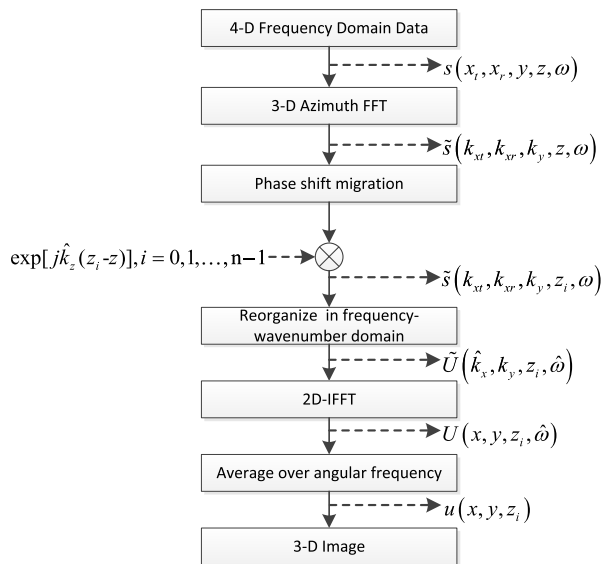
FIGURE 3. Block scheme of the proposed MIMO-SAR PSM for 3-D reconstruction.

regime,

$$\begin{cases} \delta_x \approx 0.886 \dfrac{\lambda_c z}{L_{xt} + L_{xr}} \\ \delta_y \approx 0.886 \dfrac{\lambda_c z}{2L_y} \\ \delta_z \approx 0.886 \dfrac{c}{2B} \end{cases} \tag{18}$$

B. IMPLEMENTATION DETAILS

Fig.3 is a detailed implementation procedure of the proposed MIMO-SAR PSM algorithm in accordance to (16), the FT and IFT operations of which are carried out with FFT and IFFT with high computation efficiency

Before performing FFT operations along x_t and x_r dimensions, zero-padding process shown in the following equation needs to be done to make the transmitting array and receiving array the same length in order to get the same spatial frequency interval

$$(N_{xt} - 1) \, d_{xt} = (N_{xr} - 1) \, d_{xr} \tag{19}$$

where N_{xt} and N_{xr} represent the number of zero-padding of the transmitting and receiving array respectively.

The frequency-wavenumber domain data is then phase shifted from the sampling plane z to z_i planes in the FOV with the phase shift term $\exp[j\hat{k}_z(z_i - z)]$ after performing the 3-D FFT operation.

After the phase shift operations, the distributed 5-D data $\tilde{s}(k_{xt}, k_{xr}, k_y, z_i, \omega)$ in the frequency domain of x dimension needs to be rearranged into the modified wavenumber $\hat{k}_x$ domain in accordance to the relationship defined in (9).

If two or more samples fall into the same $\hat{k}_x$, the contributions can be added or averaged to prevent information lost, which is equivalent to different windowing operations and corresponds to different performance of the PSF as well [16].

In this paper, the summation of the same $\hat{k}_x$ data is adopted to gain a relatively better sidelobe in x direction.

Hence, we obtained the rearranged data in the modified frequency-wavenumber domain with uniform $\hat{k}_x$ and k_y. The 'exploding fields' are then transformed from the frequency-wavenumber domain to the frequency-space domain by utilizing the 2-D IFFT operation. Finally, the fully focused 3-D image can be reconstructed by the integration over the 'equivalent frequencies' $\hat{\omega}$ as given in (15).

C. COMPUTATIONL COST

Table 1 illustrated the detailed computational cost of the proposed MIMO-SAR PSM algorithm. To measure more compactly, the final computational cost is evaluated by the number of floating-point operation (FLOP), which can be either a real multiplication or a real addition [24]. The final computation cost of the MIMO-SAR PSM algorithm is shown as

$$\begin{aligned} C_1 = {} & 5N_f N_{xt} N_{xr} N_y [\log_2(N_{xt} N_{xr} N_y) + 1.6N_z] \\ & + 5N_f N_z N_x N_y \log_2(N_x N_y) \, FLOP \end{aligned} \tag{20}$$

where N_f is the frequency steps number of the SFCW signal, N_x is the number of monostatic spatial frequency in the x-direction with an expression as $N_x = N_{xt} + N_{xr} - 1$, N_y is the number of scanning points in y-direction, and N_z is the number of the resulted planes in the ROI.

For comparison, the computational cost of an improved BP algorithm with FFT integrated in range domain for acceleration, as given in [26], is borrowed as

$$C_2 = 5N_{xt} N_{xr} N_y N_f \log_2 N_f + 12 N_{xt} N_{xr} N_y N_x' N_y' N_z' FLOP \tag{21}$$

where N_x', N_y', N_z' are the reconstructed points of the ROI.

The total computation cost of the MIMO-SAR RMA proposed in [24] is also shown as

$$\begin{aligned} C_3 = {} & 5N_{xt} N_{xr} N_y [N_f \log_2(N_{xt} N_{xr} N_y) + 1.2N_f + 1.6N_z] \\ & + 5N_x N_z N_y [\log(N_x N_z N_y) - 0.4] \, FLOP \end{aligned} \tag{22}$$

To further simplify the comparison, we suppose that N_y, N_f, N_z, N_x', N_y', N_z' are in the same order with a given number N. For N_{xt}, N_{xr}, since the number of EPC is determined by $N_{xt} \cdot N_{xr}$, it is more reasonable to assume that N_{xt}, N_{xr} are in the order of $\sqrt{N}$ respectively [26]. Therefore, we obtained more intuitive expressions of (20), (21) and (22), which are $O(N^4)$, $O(N^5)$ and $O(N^3 \log N)$ respectively. The great improvement in efficiency of the proposed MIMO-SAR PSM algorithm is obvious and will be further validated by simulation and experiments in the following sections.

IV. NUMERICAL SIMULATION

In this part, the MIMO-SAR PSM algorithm was verified through the comparison with the improved BP algorithm and the MIMO-SAR RMA in image quality and consumed imaging computational complexity as well.

TABLE 1. Computation cost of the MIMO-SAR PSM Algorithm.

Operation	Real multiplications	Real additions
Spatial 3-D FFT	$2N_f N_{xt} N_{xr} N_y \left(\log_2 N_{xt} + \log_2 N_{xr} + \log_2 N_y \right)$	$3N_f N_{xt} N_{xr} N_y \left(\log_2 N_{xt} + \log_2 N_{xr} + \log_2 N_y \right)$
Apply $\exp[\, j \hat{k}_z (z_i - z)]$	$4N_f N_{xt} N_{xr} N_y N_z$	$2N_f N_y N_z N_{xt} N_{xr}$
Reorganize	0	$2N_f N_y N_z \left(N_{xt} N_{xr} - N_x \right)$
Spatial 2-D IFFT	$2N_f N_z N_x N_y \left(\log_2 N_x + \log_2 N_y \right)$	$3N_f N_z N_x N_y \left(\log_2 N_x + \log_2 N_y \right)$
Average over ω^*	0	$2N_f N_y N_z N_x$
Total	$2N_f N_{xt} N_{xr} N_y \left(\log_2 N_{xt} + \log_2 N_{xr} + \log_2 N_y \right)$ $+2N_f N_z N_x N_y \left(\log_2 N_x + \log_2 N_y \right)$ $+4N_f N_{xt} N_{xr} N_y N_z$	$3N_f N_{xt} N_{xr} N_y \left(\log_2 N_{xt} + \log_2 N_{xr} + \log_2 N_y \right)$ $+3N_f N_z N_x N_y \left(\log_2 N_x + \log_2 N_y \right)$ $+4N_f N_y N_z N_{xt} N_{xr}$

Two simulations based on different targets are presented here. The first target shown in Fig.4(a) consists of 9-point scatters distributed within an area of 0.15 m × 0.15 m × 0.15 m. The second target shown in Fig.4(b) is an extended target Siemens Star with a diameter of 12 cm. The center point of these two targets is located at 1 m away from the planar aperture with an azimuth position located at the center of the planar array. The frequency of the signal centered at 0.1 THz with bandwidth 15.75 GHz sampled as 31 points in a step of 525 MHz.
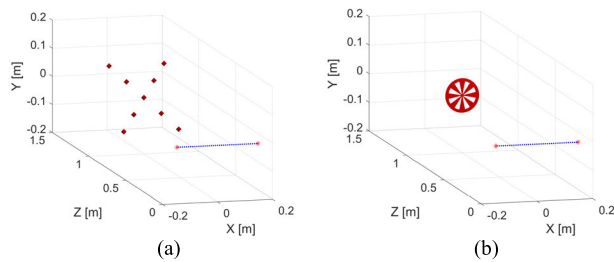

FIGURE 5. Horn antenna for simulation and experiment with detailed dimensions.

FIGURE 4. The MIMO-SAR set up used in the numerical simulation, with the 1-D MIMO array located at a distance of 1m from the target. (a) Nine distributed point scatters target in the first simulation. (b) Siemens Star target in the second simulation.

The 1-D MIMO array structure shown in Fig.4 is adopted in the following simulation with 6 transmitters and 39 receivers. The total length of the MIMO array is 0.3 m, with intervals of 2.5 mm for the transmitting elements and 7.5 mm for the receiving elements, respectively, and the scanning length of the synthetic aperture direction is 0.3 m with a spatial interval of 2 mm, which is in accordance with the Nyquist sampling criteria shown in (17). No optimization techniques for array design is adopted here, since the main focus of this paper is put on the improvement of the image reconstruction method. According to (18), the theoretical resolutions along x-direction, y-direction and z-direction under this setting are 4.5 mm, 4.4 mm and 8.4 mm, respectively.

The simulation is based on the field distribution of the horn shown in Fig.5 at the front of the transmitter and receiver

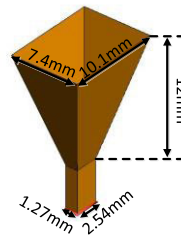in the plane at a concerned distance. With the simulated filed distribution acquired by the commercial electromagnetic computation software FEKO, the bistatic MIMO-SAR echoed data can be obtained. And then, the MIMO-SAR PSM algorithm developed in Section II was verified to reconstruct the image with high efficiency.

Fig.6 shows the reconstructed image for the 9-point targets set in Fig.4. The 3-D images have been reconstructed within a 0.2m ×0.2m ×0.2m cube. The 3-D images and its front/side views projecting onto the x-y and z-y planes of the 9-point targets are all shown. For a comprehensive comparison, the images based on the improved BP algorithm and the MIMO-SAR RMA and the MIMO-SAR PSM algorithm proposed in this paper are both given. Through the reconstructed images in Fig.6, we can find that results of the three algorithms all get fully focused. The resolutions in x-direction, y-direction and z-direction were also tested by extracting the 3-dB width of the PSF of the center point, which were 4.7 mm, 4.9 mm, and 8.1 mm, respectively, which is close to the theoretical ones.

In order to illustrate the difference more clearly, Fig.7 shows the PSFs of the three algorithms for a single point target at (0,0,1). The well consistency between them can be clearly observed, however, at the position of about 0.025m we can find a sidelobe of the MIMO-SAR RMA is about 3-dB higher than the MIMO-PSM, 6-dB higher than BP. A similar case can be also found in the second simulation results as
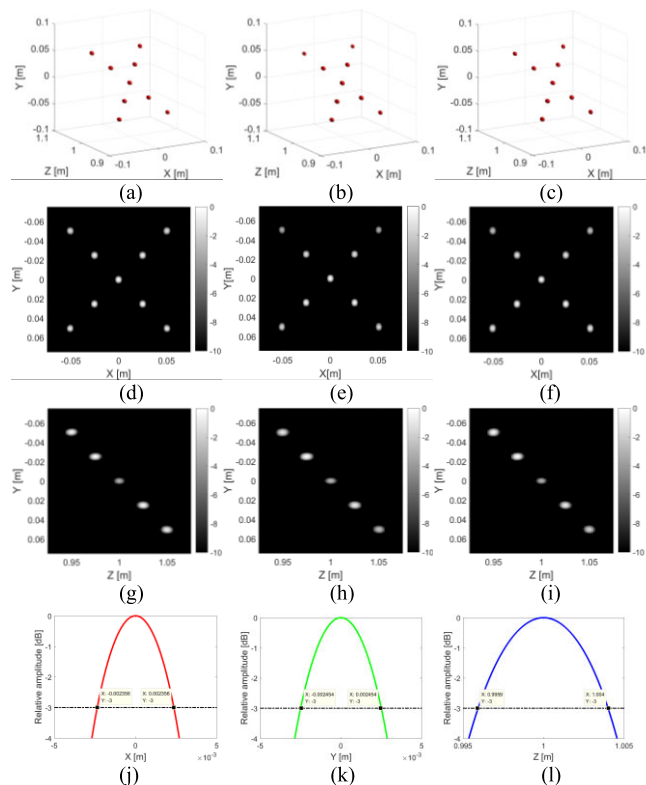
FIGURE 6. Imaging results of the first simulation shown in Fig. 4(a) with the MIMO-SAR configuration. (a) 3-D image by BP. (b) 3-D image by MIMO-SAR RMA. (c) 3-D image by MIMO-SAR PSM. (d) Front view of the image obtained by BP. (e) Front view of the image obtained by MIMO-SAR RMA. (f) Front view of the image obtained by MIMO-SAR PSM. (g) Side view by BP. (h) Side view by MIMO-SAR RMA. (i) Side view by MIMO-SAR PSM. The front/side views are obtained by maximum projection of the 3-D image on to the x-y and z-y planes, respectively. (j-l) Resolution tests of MMO-SAR PSM along x, y, and z directions, respectively.
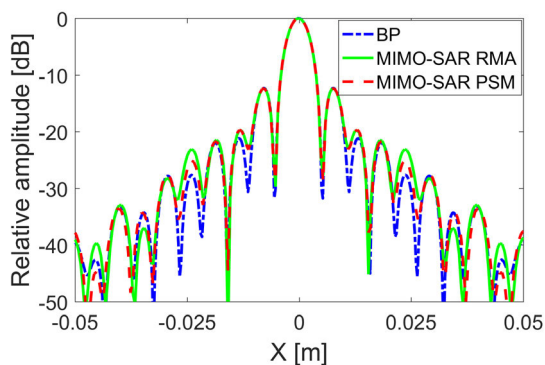

FIGURE 7. PSFs of different algorithms.

shown in Fig.8 by observing the stronger interferes between metal sectors in Fig.8(b) and Fig.8 (e).

As mentioned in [33], the time consuming of algorithms implementation depends largely on the type of computers, and different programming habits and optimization methods will also lead to different processing time even for the same algorithm. Therefore, we think it's reasonable and objective to evaluate different algorithms by their FLOP times
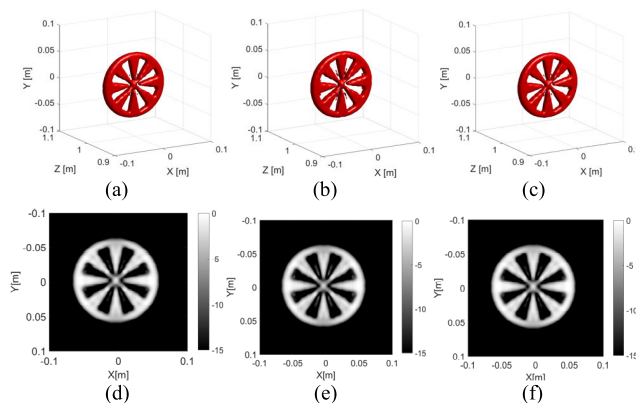

FIGURE 8. Imaging results of the second simulation shown in Fig. 4(b) with the MIMO-SAR configuration. (a) 3-D image by BP. (b) 3-D image by MIMO-SAR RMA. (c) 3-D image by MIMO-SAR PSM. (d) Front view of the image obtained by BP. (e) Front view of the image obtained by MIMO-SAR RMA. (f) Front view of the image obtained by MIMO-SAR PSM.

according to actual parameters of simulations or experiments. The number of FLOP of these three algorithms are shown in Table 2. The computational loads of these two simulations are the same due to the same simulation setup. From Table 2, we can find that the calculation amount of the proposed algorithm is on the same order as the MIMO-SAR RMA, which is much smaller than the calculation amount of BP. The final 3-D image of the entire reconstruction of the proposed algorithm takes less than 12 s which is much less than the improved BP algorithm.

TABLE 2. Comparison on computational times of different algorithms of the simulation.

Algorithms	FLOP (10^{10})
BP	2735
MIMO-SAR RMA	0.7
MIMO-SAR PSM	2.3

V. EXPERIMENT RESULTS

A. EXPERIMENT SETUP

To illustrate the performance of the proposed MIMO-SAR PSM algorithm in practical applications, as shown in Fig.9, a prototype imager was developed in the 0.1 THz band. The system was fabricated based on a microwave Vector Network Analyzer (VNA) combined with two transmitters to multiply the signal to the 0.1 THz band, and a receiver to convert the 0.1 THz signal to the intermediate frequency (IF) signal. Then the IF signal is sent to the VNA to extract its amplitude and phase information. The linear MIMO array can be equivalently realized by scanning the two transmitters and receiver along the horizonal direction (x-direction) with the help of three motor driven platform. And the moving of the whole virtual MIMO array in the vertical direction (y-direction) was controlled by the fourth motor driven platform to cover the
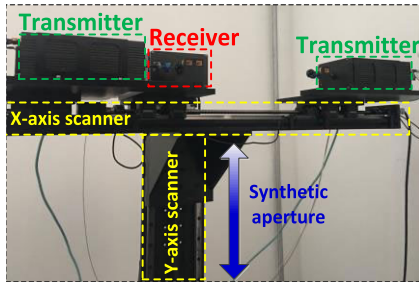
FIGURE 9. Photograph of the 2-D-scanner of the experiment setup.

FOV in SAR direction. Three identical horns with 3 dB beam width 19° are used as the transmitting and receiving antennas.

In the experimental setup, a virtual MIMO array the same as the simulation is equivalently realized as schematically shown in Fig.4. If the actual MIMO array elements are adequate, the data acquisition will be realized by switching the transmitters sequentially with the receivers receiving in parallel, without any mechanical movement along the horizontal direction. Hence, the effective synthetic aperture time can be reasonably evaluated by adding the frequency sweeping time for the transmitters in the whole imaging experiment, considering the parallel data receiving for a practical MIMO-SAR system. The time of one frequency sweeping is 2 ms in our experiment. For single MIMO scan along horizontal direction, frequency sweeping is performed sequentially at 6 transmitting positions. And the whole imaging process is composed of N_y MIMO scans corresponding to N_y positions at the synthetic aperture direction (vertical direction). Therefore, the total effective synthetic aperture time is $12N_y$ ms. And the mechanical movement in vertical direction is slightly larger than the total effective synthetic aperture time.

The complete band of this system is 75~110 GHz with a sampling step of 175 MHz. In order to avoid data redundancy, we selected 15.75 GHz experimental data in the full bandwidth, the center frequency is 0.1 THz, and the sampling step is 525 MHz, which is also consistent with the settings of the simulation.

B. EXPERIMENTAL RESULTS IN THE FREE SPACE

The target of the first experiment is a metallic letter A fixed on the absorbing material. The height of the target is 14.5 cm and the width is 16.5 cm. The distance between the target and the scanning aperture is about 1m. The vertical scanning is 50 cm with a 2 mm interval. The corresponding total effective synthetic aperture time is 3s.

High consistency between these three algorithms can be observed clearly as shown in Fig.10. However, the computational times of the 3-D reconstruction of the MIMO-SAR RMA and the proposed MIMO-SAR PSM algorithm are far less than that of the improved BP algorithm as shown in Table 3.

As can be seen in Fig.11(a)-(b), the second experiment with three different targets arranged at three different ranges
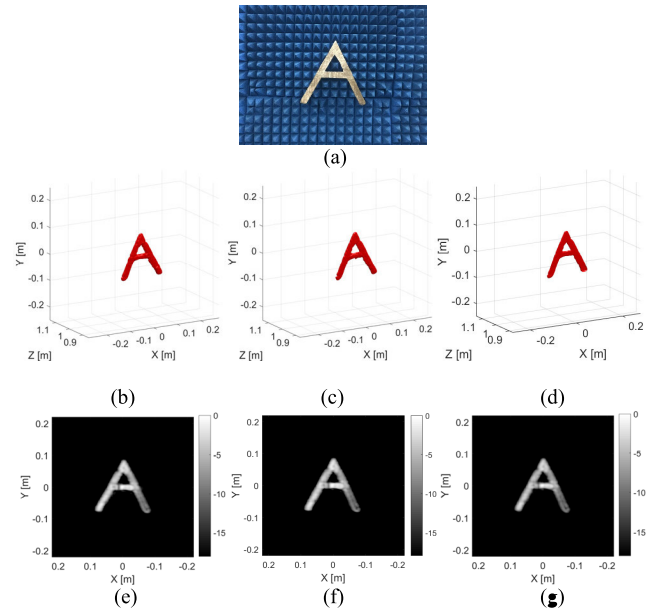

FIGURE 10. 3-D reconstructions for metallic target A. Front views are obtained by maximum projection of 3-D images onto x-y plane. (a) Photo of metallic A. (b) 3-D image by BP algorithm. (c) 3-D image by MIMO-SAR RMA. (d) 3-D image by MIMO-SAR PSM algorithm. (e) Front view of image by BP algorithm. (f) Front view of image by MIMO-SAR RMA. (g) Front view of image by MIMO-SAR PSM algorithm.

TABLE 3. Comparison on computational times needs of different algorithms of experiment I.

Algorithms	FLOP (10^{10})
BP	7556
MIMO-SAR RMA	1.2
MIMO-SAR PSM	3.9

away from the scanning aperture is also shown to validate the ability of full-adaptive focusing of the proposed MIMO-SAR PSM algorithm. Additionally, results of the BP algorithm and the MIMO-SAR RMA are also presented to make a more comprehensive comparison. The vertical scanning length in this experiment is 30 cm with 2 mm interval. The corresponding total effective synthetic aperture time is 1.8s.

The fully focused imaging results of these three algorithms can be seen in Fig.11(c)-(e), which are nearly identical. However, if we compare Fig.11(c)-(e) more carefully, we could find that a better imaging quality is obtained by the proposed algorithm than the MIMO-SAR RMA through comparing the trigger part of the gun in these two pictures, the enlarged images are presented in Fig.11(g)-(i). Cautiously, we think this is mainly due to the non-interpolation feature of the proposed algorithm which avoids the numerical error resulted from the Stolt interpolation, which is consistent with the simulation results in Fig.7 and Fig.8.

The computational times of the three different algorithms are listed on Table 4. Although the MIMO-SAR PSM algorithm needs more time than the MIMO-SAR RMA, its computational complexity is no more than 0.09% of that of the
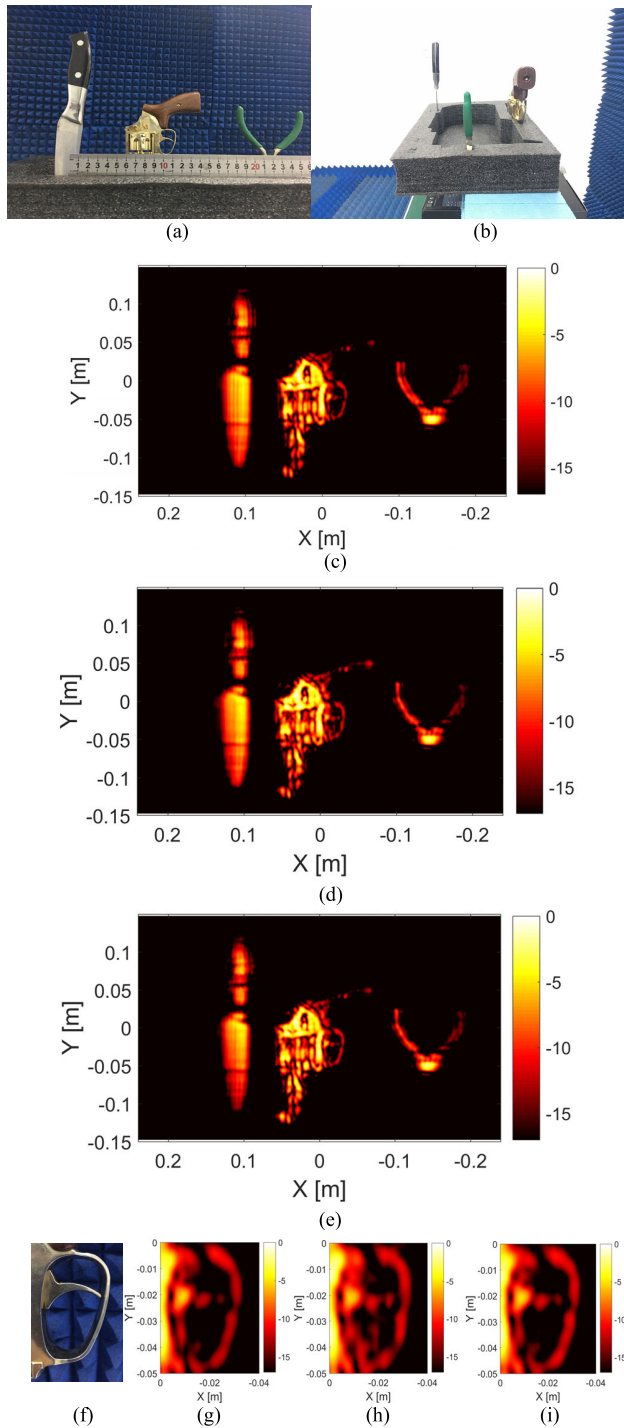
TABLE 4. Comparison on computational times needs of different algorithms of experiment II.

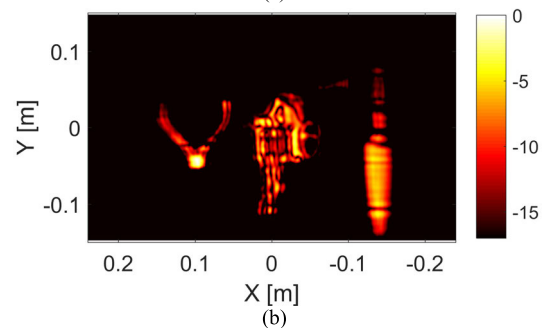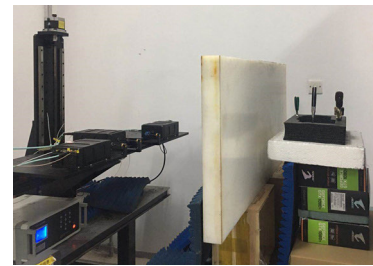| Algorithms	FLOP (10^{10})
BP	2735
MIMO-SAR RMA	0.7
MIMO-SAR PSM	2.3

FIGURE 12. Complementary experiment on multi-layer medium imaging problem. (a) Photo of the multi-layer medium imaging scene. (b) Reconstructed result by MIMO-SAR PSM algorithm.

FIGURE 11. Adaptive focusing experiment for three targets distributed in different ranges. (a) Photo of front view of three targets. (b) Photo of side view of three targets. (c) Adaptive focusing result reconstructed by BP algorithm. (d) Adaptive focusing result reconstructed by MIMO-SAR RMA algorithm. (e) Adaptive focusing result reconstructed by MIMO-SAR PSM algorithm.(f) Photo of the trigger part of the metal gun. (g) Enlarged image of the trigger part of the metal gun reconstructed by BP algorithm. (h) Enlarged image of the trigger part of the metal gun reconstructed by MIMO-SAR RMA algorithm. (i) Enlarged image of the trigger part of the metal gun reconstructed by MIMO-SAR PSM algorithm.

BP algorithm. Furthermore, taking advantages of the independence of image reconstruction on different range planes, parallel computing.

C. EXPERIMENTAL RESULTS IN THE MULTI-LAYER MEDIUM

Additionally, the proposed MIMO-SAR PSM can also be extended to deal with the image reconstruction in multi-layer medium. This was furthermore verified by another proof-of-state experiment shown in Fig.12, which has the same experimental parameter settings as experiment two. A polyethylene having a refractive index of 1.5 and a known thickness of 5.2 cm is placed in front of the targets which divided the medium in the imaging scene into three layers. The distance between the MIMO-SAR aperture and the polyethylene can be measured precisely through the scattered waves. While taking advantages of the extrapolation feature in the range direction of the proposed MIMO-SAR PSM algorithm as shown in (13), a well-focused image can still be fully focused, as shown in Fig.11(b), by substituting k and c_0 in (9) with $k' = \omega/v$ and v for the polyethylene region, where $v = c_0/n'$ is the propagating speed of electromagnetic waves in the medium and n' is the value of the refractive index. It should be noted that, in order to accelerate the image reconstruction when processing multi-layer medium problems, parallel computing can still be used in each layer separately based on the fields of the first range plane in the corresponding layer.

VI. CONCLUSION

In this paper, the extension of the PSM for 3-D MIMO-SAR imaging in THz band has been investigated based on the exploded reflector model and the wave equations. By analyzing the derived analytical expression of the scattered waves in the frequency-wavenumber domain, the relationship between the 'exploding fields' and the bistatic data recorded in MIMO-SAR was revealed, and the analytical expression of the 'explode fields' was derived from the MIMO-SAR data. The formula of the 'equivalent frequency' and the modified phase shift term was derived to establish a comprehensive MIMO-SAR PSM algorithm at the first time. By effectively employing the fast Fourier transform in the algorithm, the proposed algorithm has a great reduction on the time consuming in reconstructing the THz images as compared with the improved BP algorithm, without loss of the imaging qualities. Compared with the Stolt migration, the proposed MIMO-SAR PSM has better accuracy. Additionally, on the merits of the extrapolation feature in the range direction, PSM can be more flexibly extended for the image reconstruction in multi-layer medium. A MIMO-SAR prototype imager was designed for the proof-of-principle experiments in 0.1 THz band. 3-D imaging results of different targets were given, both in free space and in multi-layer medium case, to demonstrate the theoretical results obtained in this paper and the effectiveness and the efficiency of the proposed algorithm. Due to the current wavenumber domain algorithms for the MIMO-SAR scheme are all based on the Nyquist sampling criteria, in our future work, compressive sampling will be concerned to reduce the number of measurements, thereby reducing system costs.

REFERENCES

[1] C. Zandonella, "Terahertz imaging: T-ray specs," *Nature*, vol. 424, pp. 721–722, Aug. 2003.

[2] Z. Popovic and E. N. Grossman, "THz metrology and instrumentation," *IEEE Trans. THz Sci. Technol.*, vol. 1, no. 1, pp. 133–144, Sep. 2011.

[3] R. Appleby and H. B. Wallace, "Standoff detection of weapons and contraband in the 100 GHz to 1 THz region," *IEEE Trans. Antennas Propag.*, vol. 55, no. 11, pp. 2944–2956, Nov. 2007.

[4] Q. Song, Y. Zhao, A. Redo-Sanchez, C. Zhang, and X. Liu, "Fast continuous terahertz wave imaging system for security," *Opt. Commun.*, vol. 282, no. 10, pp. 2019–2022, May 2009.

[5] K. Cooper, R. Dengler, N. Llombart, T. Bryllert, G. Chattopadhyay, E. Schlecht, J. Gill, C. Lee, A. Skalare, I. Mehdi, and P. Siegel, "Penetrating 3-D imaging at 4- and 25-m range using a submillimeter-wave radar," *IEEE Trans. Microw. Theory Techn.*, vol. 56, no. 12, pp. 2771–2778, Dec. 2008.

[6] N. Llombart, K. B. Cooper, R. J. Dengler, T. Bryllert, and P. H. Siegel, "Confocal ellipsoidal reflector system for a mechanically scanned active terahertz imager," *IEEE Trans. Antennas Propag.*, vol. 58, no. 6, pp. 1834–1841, Jun. 2010.

[7] K. B. Cooper, R. J. Dengler, N. Llombart, B. Thomas, G. Chattopadhyay, and P. H. Siegel, "THz imaging radar for standoff personnel screening," *IEEE Trans. THz Sci. Technol.*, vol. 1, no. 1, pp. 169–182, Sep. 2011.

[8] D. M. Sheen, D. L. Mcmakin, T. E. Hall, and R. H. Severtsen, "Active millimeter-wave standoff and portal imaging techniques for personnel screening," in *Proc. IEEE Conf. Technol. Homeland Secur.*, May 2009, pp. 440–447.

[9] J. B. Jackson, J. Bowen, G. Walker, J. Labaune, G. Mourou, M. Menu, and K. Fukunaga, "A survey of terahertz applications in cultural heritage conservation science," *IEEE Trans. THz Sci. Technol.*, vol. 1, no. 1, pp. 220–231, Sep. 2011.

[10] V. Krozer, T. Löffler, J. Dall, A. Kusk, F. Eichhorn, R. K. Olsson, J. D. Buron, P. U. Jepsen, V. Zhurbenko, and T. Jensen, "Terahertz imaging systems with aperture synthesis techniques," *IEEE Trans. Microw. Theory Techn.*, vol. 58, no. 7, pp. 2027–2039, Jul. 2010.

[11] X. Gao, C. Li, S. Gu, and G. Fang, "Design, analysis and measurement of a millimeter wave antenna suitable for stand off imaging at checkpoints," *J. Infr., Millim., THz Waves*, vol. 32, no. 11, pp. 1314–1327, Nov. 2011.

[12] S. Gu, C. Li, X. Gao, Z. Sun, and G. Fang, "Terahertz aperture synthesized imaging with fan-beam scanning for personnel screening," *IEEE Trans. Microw. Theory Techn.*, vol. 60, no. 12, pp. 3877–3885, Dec. 2012.

[13] F. Friederich, W. Von Spiegel, M. Bauer, F. Meng, M. D. Thomson, S. Boppel, A. Lisauskas, B. Hils, V. Krozer, A. Keil, T. Loffler, R. Henneberger, A. K. Huhn, G. Spickermann, P. H. Bölivar, and H. G. Roskos, "THz active imaging systems with real-time capabilities," *IEEE Trans. THz. Sci. Technol.*, vol. 1, no. 1, pp. 183–200, Sep. 2011.

[14] T. A. Reck, J. Siles, and C. Jung, "Array technology for terahertz imaging," *Proc. SPIE*, vol. 8362, May 2012, Art. no. 836202.

[15] K. B. Cooper, T. A. Reck, and C. Jung, "Transceiver array development for submillimeter-wave imaging radars," *Proc. SPIE*, vol. 8715, May 2013, Art. no. 87150A.

[16] H. Gao, C. Li, S. Zheng, S. Wu, and G. Fang, "Implementation of the phase shift migration in MIMO-sidelooking imaging at terahertz band," *IEEE Sensors J.*, vol. 19, no. 20, pp. 9384–9393, Oct. 2019, doi: 10.1109/jsen.2019.2925461.

[17] N. E. Alexander, B. Alderman, F. Allona, P. Frijlink, R. Gonzalo, M. Hägelen, A. Ibáñez, V. Krozer, M. L. Langford, E. Limiti, D. Platt, M. Schikora, H. Wang, and M. A. Weber, "TeraSCREEN: Multi-frequency multi-mode Terahertz screening for border checks," *Proc. SPIE*, vol. 9078, Jun. 2014, Art. no. 907802.

[18] J. Gao, Z. Cui, B. Cheng, Y. Qin, X. Deng, B. Deng, X. Li, and H. Wang, "Fast three-dimensional image reconstruction of a standoff screening system in the terahertz regime," *IEEE Trans. THz Sci. Technol.*, vol. 8, no. 1, pp. 38–51, Jan. 2018.

[19] S. Ahmed, A. Schiessl, F. Gumbmann, M. Tiebout, S. Methfessel, and L.-P. Schmidt, "Advanced microwave imaging," *IEEE Microw.*, vol. 13, no. 6, pp. 26–43, Sep. 2012.

[20] X. Zhuge, A. G. Yarovoy, T. Savelyev, and L. Ligthart, "Modified kirchhoff migration for UWB MIMO array-based radar imaging," *IEEE Trans. Geosci. Remote Sens.*, vol. 48, no. 6, pp. 2692–2703, Jun. 2010.

[21] X. Zhuge and A. G. Yarovoy, "A sparse aperture MIMO-SAR-based UWB imaging system for concealed weapon detection," *IEEE Trans. Geosci. Remote Sens.*, vol. 49, no. 1, pp. 509–518, Jan. 2011.

[22] F. Gumbmann and L.-P. Schmidt, "Millimeter-wave imaging with optimized sparse periodic array for short-range applications," *IEEE Trans. Geosci. Remote Sens.*, vol. 49, no. 10, pp. 3629–3638, Oct. 2011.

[23] X. Zhuge and A. G. Yarovoy, "Three-dimensional near-field MIMO array imaging using range migration techniques," *IEEE Trans. Image Process.*, vol. 21, no. 6, pp. 3026–3033, Jun. 2012.

[24] R. Zhu, J. Zhou, G. Jiang, and Q. Fu, "Range migration algorithm for near-field MIMO-SAR imaging," *IEEE Geosci. Remote Sens. Lett.*, vol. 14, no. 12, pp. 2280–2284, Dec. 2017.

[25] T. Olofsson, "Phase shift migration for imaging layer objects and objects immersed in water," *IEEE Trans. Ultrason., Ferroelectr., Freq. Control*, vol. 57, no. 11, pp. 2522–2530, Nov. 2010.

[26] J. Gao, Y. Qin, B. Deng, H. Wang, and X. Li, "Novel efficient 3D short-range imaging algorithms for a scanning 1D-MIMO array," *IEEE Trans. Image Process.*, vol. 27, no. 7, pp. 3631–3643, Jul. 2018.

[27] D. Loewenthal, L. Lu, R. Roberson, and J. Sherwood, "The wave equation applied to migration," *Geophys. Prospecting*, vol. 24, no. 2, pp. 380–399, Jun. 1976.

[28] J. Gazdag, "Wave equation migration with the phase–shift method," *Geophysics*, vol. 43, no. 7, pp. 1342–1351, Dec. 1978.

[29] J. F. Claerbout, "Imaging the Earth's interior," *Geophys. J.. Roy. Astron. Soc.*, vol. 86, no. 1, p. 217, Jul. 1986.

[30] S. Gu, C. Li, X. Gao, Z. Sun, and G. Fang, "Three-dimensional image reconstruction of targets under the illumination of terahertz Gaussian Beam–theory and experiment," *IEEE Trans. Geosci. Remote Sens.*, vol. 51, no. 4, pp. 2241–2249, Apr. 2013.

[31] K. Gu, G. Wang, and J. Li, "Migration based SAR imaging for ground penetrating radar systems," *IEE Proc., Radar Sonar Navig.*, vol. 151, no. 5, p. 317, 2004.

[32] I. G. Cumming and F. H. Wong, *Digital Processing of Synthetic Aperture Radar Data: Algorithms and Implementation*. Norwood, MA, USA: Artech House, 2004.

[33] D. Sheen, D. Mcmakin, and T. Hall, "Three-dimensional millimeter-wave imaging for concealed weapon detection," *IEEE Trans. Microw. Theory Techn.*, vol. 49, no. 9, pp. 1581–1592, Sep. 2001.

[34] S. S. Ahmed, A. Schiessl, and L.-P. Schmidt, "A novel fully electronic active real-time imager based on a planar multistatic sparse array," *IEEE Trans. Microw. Theory Techn.*, vol. 59, no. 12, pp. 3567–3576, Dec. 2011.

HANG GAO received the B.E. degree from Northwestern Polytechnical University, Xi'an, China, in 2015. He is currently pursuing the Ph.D. degree with the Aerospace Information Research Institute, Chinese Academy of Sciences (CAS), Beijing, China.

His research interests include radar signal processing and millimeter-wave and terahertz imaging technology.

CHAO LI received the B.S. degree in physics from Qingdao Ocean University, Qingdao, China, in 2000, and the M.S. and Ph.D. degrees in electrical engineering from the Chinese Academy of Sciences (CAS), Beijing, China, in 2003 and 2008, respectively.

Since 2004, he has been with the Key Laboratory of Electromagnetic Radiation and Sensing Technology, CAS, where he became a Professor and currently leads a group on the research of terahertz imaging theory and technology with projects supported by the National Natural Science Foundation of China, National High Technology Research and Development Projects (863 Projects) of China, and the National Key Research and Development Program of China. He has authored or coauthored more than 80 peer-reviewed articles. Since 2019, he has also been with the Aerospace Information Research Institute, CAS. He authored one book. His research interests include terahertz imaging technology, antenna and wave propagation, computational electromagnetics, and artificial metamaterials in microwave and terahertz bands.

Dr. Li was a recipient of numerous awards and honors, including the 2009 Outstanding Doctoral Dissertation Award, CAS, the 2010 National One-Hundred Excellent Doctoral Dissertation Nomination Award, the 2010 Advanced Researcher of 863 Projects, and the 2012 Lu Jiaxi Young Talent Award.
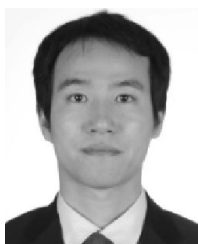
SHIYOU WU received the B.E. degree in electronic engineering from Anhui Normal University, Anhui, China, in 2007, and the Ph.D. degree from the Institute of Electronics, Chinese Academy of Sciences (CAS), Beijing, China, in 2012.

Since 2012, he has been with the Key Laboratory of Electromagnetic Radiation and Sensing Technology, CAS. His main research interests are in the areas of UWB through-wall radar detection, imaging, life detection, and other related applications.

HEBIN GENG received the B.E. degree from the Huazhong University of Science and Technology, Wuhan, China, in 2017. He is currently pursuing the M.S. degree with the Aerospace Information Research Institute, Chinese Academy of Sciences, Beijing, China.

His research interests include THz quasi-optical scanning method, computational electromagnetic, and antenna design.

SHEN ZHENG received the B.E. degree in electromagnetic field and wireless technology from the University of Electronic Science and Technology of China, Chengdu, China, in 2014. He is currently pursuing the Ph.D. degree in electromagnetic field and microwave technology with the Institute of Electronics, Chinese Academy of Sciences (CAS), Beijing, China.

His research interests include terahertz antennas, quasi-optics, and imaging methods.
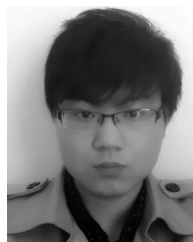
XIAODONG QU received the B.S. degree from Xidian University, Xi'an, China, in 2012, and the Ph.D. degree from the Institute of Electronics, Chinese Academy of Sciences, Beijing, China, in 2017.

His current research interests include radar signal processing and array imaging.

GUANGYOU FANG received the B.S. degree in electrical engineering from Hunan University, Changsha, China, in 1984, and the M.S. and Ph.D. degrees in electrical engineering from Xi'an Jiaotong University, Xi'an, China, in 1990 and 1996, respectively.

From 1990 to 1999, he was an Engineer, an Associate Professor, and a Professor with the China Research Institute of Radiowave Propagation. From 2000 to 2001, he was a Visiting Scholar with the University of Trieste, Trieste, Italy, and with the International Center for Science and High Technology, United Nations Industrial Development Organization, Trieste, Italy. From 2001 to 2003, he was a Special Foreign Research Fellow of the Japan Society for the Promotion of Science, working with Tohoku University, Sendai, Japan. Since 2004, he has been a Professor with the Institute of Electronics, Chinese Academy of Sciences (CAS), Beijing, China, and the Director of the Key Laboratory of Electromagnetic Radiation and Sensing Technology. Since 2019, he has also been with the Aerospace Information Research Institute, CAS. He has authored or coauthored more than 300 publications. His research interests include ultrawideband radar, ground-penetrating radar signal-processing and identification methods, terahertz imaging technology, and computational electromagnetics.

● ● ●